Extension of high power deuterium operation of negative ion based neutral beam injector in the large helical device

Extension of High Power Deuterium Operation of Negative Ion Based Neutral Beam Injector in the Large Helical Device

K. Ikeda,[1, a)] K. Tsumori,[1, 2] K. Nagaoka,[1, 3] H. Nakano,[1, 2] M. Kisaki,[1, 2] Y. Fujiwara,[1] S. Kamio,[1] Y. Haba,[3] S. Masaki,[2] and M. Osakabe[1, 2]

[1)]*National Institute for Fusion Science (NIFS), National Institutes of Natural Sciences, 322-6 Oroshi, Toki, 509-5292, Japan*

[2)]*The Graduate University for Advanced Studies, SOKENDAI, 322-6 Oroshi, Toki, 509-5292, Japan*

[3)]*Graduate School of Science, Nagoya University, Nagoya 464-8603, Japan*

(Dated: 24 August 2020)

Second deuterium operation of the negative ion based neutral beam injector (N-NBI) was performed in 2018 in the Large Helical Device (LHD). The electron and the ion current ratio improves to $I_e/I_{acc(D)} = 0.31$ using the short extraction gap distance of 7 mm between the plasma grid (PG) and the extraction grid (EG). The strength of the magnetic field by the electron deflection magnet (EDM) installed in the EG increases 17% at the PG ingress surface, which effectively reduces electron component in the negative ion rich plasma in the vicinity of PG apertures. The reduction of the electron current made it possible to operate a high power arc discharge and beam extraction. Then the deuterium negative ion current increases to 55.4 A with the averaged current density of 233 A/m^2. The thermal load on the extraction grid using 7 mm gap distance is 0.6 times smaller than the thermal load using 8 mm gap caused by the reduction of co-extracted electron current. The injection beam power increases to 2.9 MW in the beam line BL3, and the total beam injection power increases to 7 MW by three beam lines in the second deuterium campaign.

I. INTRODUCTION

A negative ion based neutral beam injector (N-NBI) which enables high energy beam injection provides the heating power for fusion required for central heating and current drive in high density torus plasma. The 500 keV N-NBI[? ?] and the 180 keV N-NBI[? ? ? ? ?] using a filament-arc discharge type negative ion source have contributed as heating sources for high ion temperature plasma generation in the JT-60U and the Large Helical Device (LHD), respectively. Currently, a 1 MeV N-NBI system for ITER[? ?] using an RF type negative ion source is under construction. Negative ion production by RF discharge was demonstrated in BATMAN[?] and ELISE[? ?], and testing with SPIDER was initiated in 2018[?]. An actual size 1 MeV N-NBI testbed MITICA for ITER is under construction in Padova[? ?]. In the negative ion source for N-NBI, electrons are extracted simultaneously with the negative ions from the ion source. When these co-extracted electrons enter the accelerator and are accelerated, an electrode is damaged by applying a large thermal load. Therefore, it is important to keep the co-extracted electron current as low as possible in the negative ion source. The N-NBI for ITER will require co-extracted electron current less than the extracted deuterium negative ion current[? ? ?].

On the other hand, the filament-arc type negative ion source has stably operated using hydrogen for many years in LHD-NBI. The injection beam power is 5 MW with the 80 A acceleration drain current of negative hydrogen ions ($I_{acc(H)}$) by two ion sources as the design value[?]. The average negative ion current density of 340 A/m^2 was achieved using slot grounded grid[?], and the ratio of electron current (I_e) to the negative ion current ($I_e/I_{acc(H)}$) was maintained 0.2 - 0.3 in the high power operation. Here, I_e is defined by subtracting the $I_{acc(H)}$ from the extraction current (I_{ext}). Deuterium discharge experiment was initiated in LHD in 2017. Three N-NBI injectors also initiated deuterium operation using an ion source optimized for hydrogen. As a result, in deuterium operation, a clear increase of the electron current to the deuterium current ($I_e/I_{acc(D)}$) was observed in the high arc power[?]. The averaged $I_e/I_{acc(D)}$ was 0.38 when the $I_{acc(D)}$ is 46 A with the arc power of 370 kW by two ion sources. Further high power deuterium operation was limited by increase of thermal load on the grid system owing to the increase of co-extracted electron current. In the second deuterium operation campaign in 2018, the $I_e/I_{acc(D)}$ was greatly reduced by modifying the accelerator gap distance, and the injection beam power was improved by increase of negative ion current using high arc discharge power for deuterium.

In this paper, the structure of the accelerator and the role of electron deflection magnetic field in electron suppression are explained. Then, the progress of negative ion current with a low co-extracted electron current will be shown. Finally, we report the reduction of the thermal load of the electrode and the increase of injection beam power in the second deuterium campaign in LHD.

II. MODIFICATION OF BEAM ACCELERATOR

Figure 1 shows the cross-section of the beam accelerator of the negative ion source for third N-NBI (BL3) in LHD. In this figure, the upper side is the arc chamber direction, and the lower side is the beam accelerating direction. The accelerator consists of 4 grids, each divided into 5 segments. The beam extraction area is a rectangle with a height of 1.2 m and a width of 0.25 m. The plasma grid (PG) is equipped with

[a)]Electronic mail: ikeda.katsunori@nifs.ac.jp

770 apertures which is a circle with a diameter of 14 mm. The electric potential of the arc chamber including PG is -180 kV. The extraction grid (EG) and the steering grid (SG) are combined at the same potential (-170 kV). The EG has a circular structure at the entrance and the inner groove removes co-extracted electrons and secondary electrons[?] . There are permanent electron deflection magnets (EDM) inside the EG which removes co-extracted electrons by bending with a magnetic field between the PG and the EG. The thermal load into the EG is removed by cooling water. Beamlets of negative ion are also deflected slightly by the EDM field between the PG and the EG. This beam deflection angle is canceled by the aperture displacement for SG[? ?] . The slot type grounded grid (GG) is used in the ion source[?] . The size of the slot is 260 mm width and 14 mm height, and 55 slots are equipped in the GG. Fourteen beamlets extracted from the EG pass through the one slot. The aperture ratio of the slot area is 0.76 with respect to the beam extraction area in the one segment of GG, which is higher than the conventional aperture type GG (16mm diameter $\times$ 770 apertures : aperture ratio 0.5). Since the long axis of the slot coincides with the beamlet deflection direction, the thermal load of GG is insensitive to the beam steering angle. Therefore, it is possible to reduce the thermal load caused by the peripheral components of the beamlet, which is a problem with the aperture type. Then the high aperture ratio contributes to the improvement of the beam current[?] . The thermal load into the GG is also removed by cooling water.

Recently, diagnostics for a negative ion and an electron in the vicinity of the PG surface have been installed to the half-scale research and development ion source (RNIS) in the test stand, and the relationship between the behavior of negative ions and electrons near the PG and the EDM field has been clarified. According to the negative ion density measurement using cavity-ring-down, an increase in the hydrogen negative ion density was observed after cesium (Cs) seeding due to the effect of PG surface production[?] . As the hydrogen negative ion density increased, the electron density decreased in the vicinity of the PG. Then, negative ion rich plasma composed of positive ions and negative ions was formed. The positive and negative saturation currents flowing into the electrostatic probe were the same[?] . The spatial distribution of the saturation current near the PG aperture measured with a spatial scanning electrostatic probe indicated that negative ion rich plasma was existing in the region inside the lobe of the EDM field[? ?] . Therefore, the negative saturation current increased outside the EDM field lobe due to the increase in electrons. In addition, it was confirmed that the origin of extracted negative ions were concentrated within 20 mm near the PG aperture by a 2D optical diagnostic and a photo-detachment diagnostic[? ?] . This result indicates that the EDM field which entered the PG ingress surface maintains negative ion rich plasma by shielding electrons from the discharge region, which effectively suppress the co-extracted electrons in negative ion beam.

According to the above discussion, the electron suppression effect is verified by modifying the EDM field in deuterium operation. In the first deuterium operation, the gap distance between PG and EG (G_{ext}) was 8 mm. This gap distance was set to 7 mm (see Fig. 1) in the second deuterium operation in 2018. Figure 2 shows the calculated magnetic field strength distribution on the PG ingress surfaces with G_{ext} = 8 mm and G_{ext} = 7 mm. In the 7 mm gap, the magnetic field strength due to EDM increases to 20.5 mT. This is an increase of 17% from 17.5 mT at 8 mm gap setting. An extraction voltage of 10 kV is applied between PG and EG, but the insulation distance in vacuum is maintained. This short gap distance applies only to the BL3 and is used for beam injection in the 2018 LHD experiment. The performance of this accelerator is evaluated from data of over 17,000 operations including the beam conditioning period and the beam injection period.

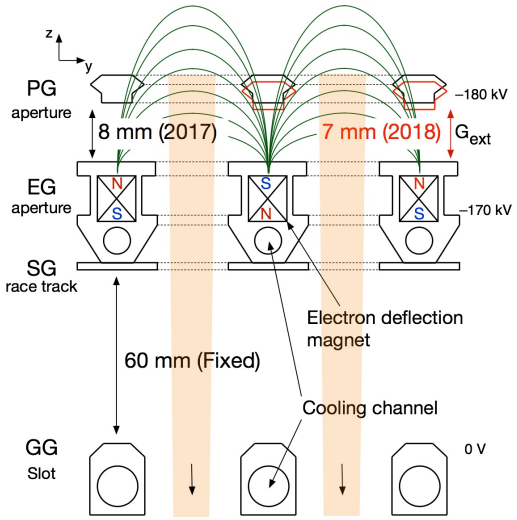

FIG. 1. The cross-sectional drawing of the beam accelerator of the negative ion source in the N-NBI (BL3). The extraction gap distance (G_{ext} : PG - EG) is modified from 8 mm to 7 mm in the second deuterium operation in 2018. The acceleration gap distance (G_{acc} : SG - GG) is fixed at 60 mm in all deuterium operations.

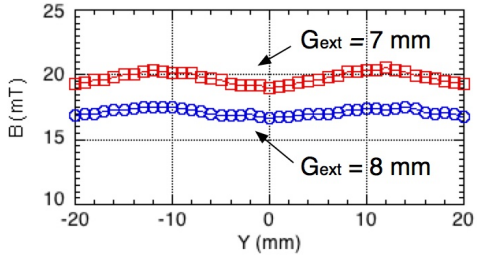

FIG. 2. Distribution of the magnetic field strength on the PG ingress surface. Squares and circles are the case of G_{ext} = 7 mm and G_{ext} = 8 mm, respectively.

III. IMPROVING EXTRACTED BEAM CURRENT AND INJECTION BEAM POWER

Figure 3 shows the result of $I_e/I_{acc(D)}$ in the deuterium beam operation. Square mark and circle mark indicate 8 mm and 7 mm G_{ext} gap, respectively. The horizontal axis represents the total arc discharge power using two ion sources. The

filling gas pressure in the arc chamber is set at 0.43 Pa and the 5 - 6 V positive bias voltage is applied, which is effective for reducing electron density in the vicinity of PG surface. The filling gas pressure and the bias voltage settings are almost the same in the two deuterium campaigns with different G_{ext} gap. A lower limit line is clearly observed in $I_e/I_{acc(D)}$ which appears under conditions of the lowest I_e and the highest $I_{acc(D)}$. The $I_e/I_{acc(D)}$ approaches this lower line with increasing negative ion density after Cs seeding. The best $I_e/I_{acc(D)}$ using the short gap of G_{ext} = 7 mm is 0.28 with 180 kW arc discharge (360 kW in Fig. 3), which is 0.74 times smaller than the $I_e/I_{acc(D)}$ using the gap of G_{ext} = 8 mm. Therefore, the reduction of the electron current due to the enhancement of EDM field enables the application of higher arc discharge power (> 200 kW/source). The $I_e/I_{acc(D)}$ is maintained at 0.31 in deuterium discharge with the arc power of 210 kW, which is as low as the usual operation range of co-extracted electron ($0.2 < I_e/I_{acc(H)} < 0.3$) in hydrogen discharge[?] .

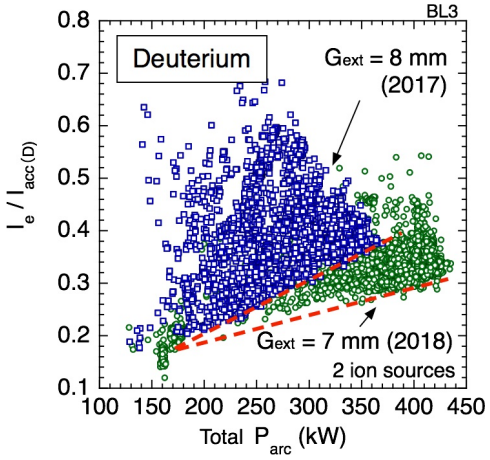

FIG. 3. The averaged $I_e/I_{acc(D)}$ using two ion sources in the deuterium operation. The horizontal axis is total arc discharge power. Squares and circles are the case of G_{ext} = 8 mm and G_{ext} = 7 mm, respectively.

Figure 4 shows the result of $I_{acc(D)}$ when increasing the arc discharge power. The $I_{acc(D)}$ increases to 55.4 A with an average arc power of 200 kW (400 kW in Fig. 4) using a gap distance of 7 mm. The average current density corresponds to 233 A/m^2. Since the $I_{acc(D)}$ was 46 A in deuterium operation with an 8 mm gap, $I_{acc(D)}$ improves 1.2 times by increase of arc discharge power with maintaining low $I_e/I_{acc(D)}$ = 0.31. The negative ion current is not saturated, and the negative ion current may further increase as the arc power increases. However, the arc power efficiency for $I_{acc(D)}$ is the same regardless of the gap distance. It can be considered that the increase in EDM field has no significant influence on the production of negative ions. Therefore, to obtain higher current in the future, it is necessary to improve the arc efficiency by another method.

On the other hand, the reduction of the co-extracted electron current results in a clear reduction of the thermal load on the electrode. Figure 5 shows a comparison of the thermal load of the EG for a 2 s deuterium beam extraction. The

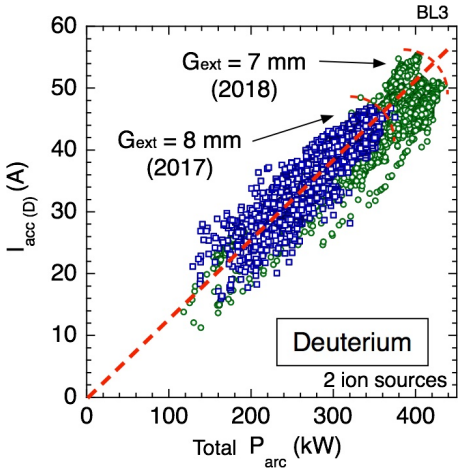

FIG. 4. The total $I_{acc(D)}$ using two ion sources in the deuterium operation. The horizontal axis is total arc discharge power. Squares and circles are the case of G_{ext} = 8 mm and G_{ext} = 7 mm, respectively.

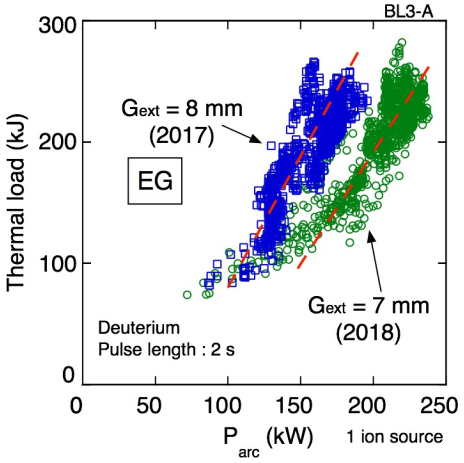

FIG. 5. The thermal load of EG for 2 s beam extraction measured by water calorimetry for the single ions source (IS3A). The horizontal axis is the arc discharge power. Squares and circles are the case of G_{ext} = 8 mm and G_{ext} = 7 mm, respectively.

square mark and the circle mark indicate an 8 mm and a 7 mm G_{ext} gap, respectively. The EG has a built-in cooling water channel (see Fig. 1), which derives the thermal load on the EG from the temperature rise of the cooling water. Since the thermal load of the EG is measured for each ion source, the thermal load of one ion source (IS3A) is plotted in Fig. 5, where the horizontal axis is the arc power of single ion source. When a negative ion beam is extracted using a 170 kW arc discharge with a gap distance of 8 mm, a thermal load of approximately 230 kJ flows into the EG due to the co-extracted electron. In the 7mm gap setting, the thermal load due to co-extracted electrons output from the ion source using the same 170 kW arc discharge power decreases to 140 kJ. Therefore, the thermal load reduction rate is 0.6. This reduction in thermal load is effective, and of course the EG surface was not damaged after the second campaign with high power beam operation. The thermal load of EG is proportional to the co-

extracted electron current, and the observed 230 kJ thermal inflow is introduced by an electron current of 8 A. This rate does not change for the gap distance. Therefore, even with a gap of 7 mm, the same 230 kJ thermal inflow requires an electron current of 8 A. Therefore, 220 kW arc discharge is required to extract this electron current using short gap. The average negative ion current extracted should be 25 A simultaneously.

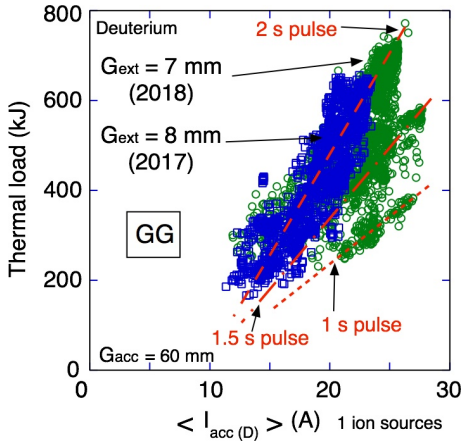

FIG. 6. The thermal load of GG for 1 s - 2 s beam extraction measured by water calorimetry for single ions source (IS3A). The horizontal axis is the averaged acceleration current. Squares and circles are the case of G_{ext} = 8 mm and G_{ext} = 7 mm, respectively.

Figure 6 shows the thermal load of GG against the averaged acceleration current $<I_{acc(D)}>$. The square mark and the circle mark indicate an 8 mm and a 7 mm G_{ext} gap, respectively. Since the acceleration power supply is commonly used by the two ion sources, the $<I_{acc(D)}>$ is evaluated as half of the acceleration current. The thermal load of GG depends on the $I_{acc(D)}$, and does not depend on the co-extracted electron current. The relationship between the $I_{acc(D)}$ and the thermal load on the GG is not changed by difference of the extraction gap distance for 1 mm. The thermal load on GG is 700 kJ at 2 s beam pulse width with the $<I_{acc(D)}>$ = 25 A. The reason for the GG thermal load is the peripheral beam component generated by the beam divergence in the short axis direction of the slot. Although this peripheral beam component is in contact with the inner wall of the GG slots, the electrode is not damaged by sufficient cooling to remove the thermal load. As the beam pulse width increases, the thermal load of the GG increases linearly as shown in Fig. 6. The maximum deuterium beam current of 55.4 A is achieved with 1.5 s beam injection using two ion sources. The characteristics of the thermal load of GG for the acceleration current of hydrogen beam and deuterium beam are the same. In the case of hydrogen, there is a heat load of 1000 kJ for the $<I_{acc(H)}>$ = 40 A, therefore the thermal load on GG is not a problem in deuterium operation with small negative ion current. In deuterium operation, a reduction in thermal load has the effect of reducing the number of electrical breakdowns between electrodes, which effect provides stable beam operation.

The perveance matching of the beam is set by minimized half beam width (FWHM) measured by a beam calorimeter at 8.3 m downstream of the ion source. This beam width includes components of beam divergence and deflection correction along the long axis of the slot. In the case of a hydrogen beam, the FWHM was 150 mm with respect to the beam extraction width of 260 mm. However, the FWHM increased to 175 mm due to an incorrect horizontal beam deflection for deuterium operation for normal gap (G_{ext} = 8 mm). The increase in FWHM is equivalent to 3 mrad converted to the divergence angle. The FWHM increases to 188 mm in the deuterium operation using short gap (G_{ext} = 7 mm). This increase in FWHM does not affect the thermal load on the GG (see Fig. 6) because the direction of the deflection is along the slot axis. Therefore, it is considered that there is no significant change in the vertical beam divergence angle along the short axis of the slot which is less than the horizontal beam deflection angle. If a conventional multi-aperture is used in GG, the mismatched beam deflection causes a large thermal load. Correction of beam deflection angle must be required in deuterium.

IV. SUMMARY OF DEUTERIUM BEAM OPERATION IN TWO YEARS

Figure 7 shows the results of $I_e/I_{acc(D)}$ and the beam injection power for the three beam lines in the first (2017) and second (2018) deuterium operations. Here, the beam injection power to the LHD is evaluated from a thermal load measurement by thermocouples installed in a carbon armor tile located on the inner wall of the LHD vacuum vessel[?] . The standard beam pulse width is 2 s, which is changed between 1 s and 2 s according to the experiment menu. The total injection beam power increased from 6.3 MW to 7 MW by three N-NBIs in 2018.

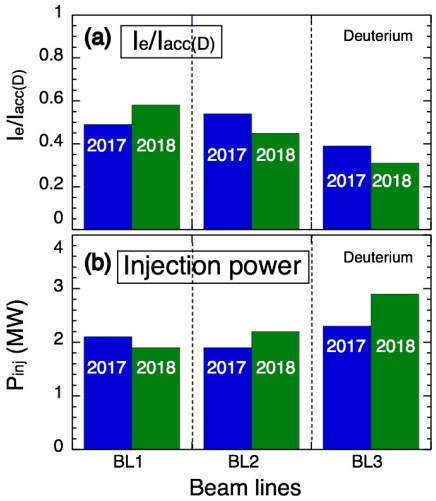

FIG. 7. (a) The $I_e/I_{acc(D)}$ and (b) the injection beam power for all N-NBIs in the deuterium operation campaigns in 2017 and 2018.

The BL3 is the most advanced deuterium support in LHD N-NBI at present. The co-extracted electron current is im-

proved by the electron suppression effect by EDM field with a short 7 mm G_{ext} gap, and $I_e/I_{acc(D)}$ decreases from 0.38 to 0.31 as shown in Fig 7(a). This improvement makes a 2.9 MW deuterium beam injection using high arc discharge power as shown in Fig. 7(b). The $I_{acc(D)}$ increases from 46 A to 55.4 A in the second deuterium operation. This improvement contributes to an increase in the total deuterium beam heating power in LHD. In order to obtain more deuterium negative ion current, it is necessary to improve the arc efficiency. In the next, third experimental campaign, the distance between the magnetic filter and the PG inside the arc chamber will change to affect the deuterium negative ion current. On the other hand, the beam width of the deuterium beam is 1.3 times wider than that of the hydrogen beam. This is because the mismatched beam deflection by SG in the accelerator is excessive for deuterium. We plan to update this problem in the near future, combining the design of the accelerator optimizing deuterium together with improving the beam current after the test using RNIS in the test stand.

The first beam line (BL1) is optimized for high power beam operation using hydrogen, which is necessary in the LHD high ion temperature experimental scenario. The beam accelerator also uses a slot type GG. The $I_{acc(H)}$ increased to 84 A by two ion sources with the low $I_e/I_{acc(H)}$ of 0.22. The hydrogen injection beam power increased to 6.1 MW in 2018. However, electron filtering in the vicinity of PG was considered to be insufficient in deuterium operation. Therefore, $I_e/I_{acc(D)}$ increases to 0.58 as shown in Fig. 5. Deuterium operation is limited due to the thermal load of the EG. In the next, third experimental campaign, the BL1 will use shorter G_{ext} gap and increase EDM field strength for deuterium operation. It is also planned to reduce co-extracted electrons by modifying the structure of the PG.

The second beam line (BL2) has the same arc discharge chamber for the ion source of the BL3. However the BL2 used a conventional aperture type GG in 2017. This was a conservative decision to focus on the stable beam operation in the first deuterium campaign, because the beam injection direction of the BL2 is different from the direction of the other two beam lines, and it has a role of toroidal current limitation in LHD. The accelerator of the BL2 replaces aperture type GG with slot type GG in 2018. The $I_e/I_{acc(D)}$ decreased to 0.45 and beam injection power increased to 2.2 MW as shown in Fig 5. In the next, third experimental campaign, it is planned to increase the deuterium beam power using a short 7 mm G_{ext} gap which is the same setting of the ion source in BL3. From these optimizations, it is expected that the 8 - 9 MW deuterium beam power will be injected by three N-NBI in the next LHD experiment.

ACKNOWLEDGMENTS

We would like to thank the technical staffs of NBI and LHD for their operational support. This research is supported by the budget for the NIFS No. ULRR702.

[1] M. Kuriyama, N. Akino, N. Ebisawa , L. Grisham, H. Liquen, A. Honda, T. Itoh *et al.,* J. of Nucl. Sci. and Technology **35**, 739 - 749 (1998).
[2] A. Kojima, M. Hanada, Y. Tanaka, M. Kawai, N. Akino, M. Kazawa, M. Komata, K. Mogaki *et al.,* Nucl. Fusion **51**, 083049 (2011).
[3] A. Iiyoshi, A. Komori, A. Ejiri, M. Emoto, H. Funaba, M. Goto, K. Ida, H. Idei, S. Inagaki *et al.,* Nucl. Fusion **39**, 1245 (1999).
[4] O. Kaneko, Y. Takeiri, K. Tsumori, Y. Oka, M. Osakabe, K. Ikeda, K. Nagaoka, T. Kawamoto, E. Asano, and M. Sato, Nucl. Fusion **43**, 692 (2003).
[5] Y. Takeiri, O. Kaneko, K. Tsumori, Y. Oka, M. Osakabe, K. Ikeda, E. Asano, T. Kawamoto, and R. Akiyama, Rev. Sci. Instrum. **71**, 1225 (2000).
[6] K. Tsumori, K. Nagaoka, M. Osakabe, Y. Takeiri, K. Ikeda, O. Kaneko, Y. Oka, T. Kawamoto *et al.,* Rev. Sci. Instrum. **75**, 1847 (2004).
[7] T. Mutoh, K. Nagaoka, H. Takahashi, H. Kasahara, M. Osakabe, S. Kubo, T. Shimozuma *et al.,* Fusion Science and Technology **68**, 216 (2015).
[8] R. Hemsworth, A. Tanga, and V. Antoni, Rev. Sci. Instrum. **79**, 02C109 (2008).
[9] M. J. Singh, D. Boilson, A. R. Polevoi, T. Oikawa, and R. Mitteau, New J. Phys. **19**, 055004 (2017).
[10] P. Franzen, H.D. Falter, E. Speth, W. Kraus, M. Bandyopadhyay, A. Encheva, U. Fantz, Th. Franke *et al.,* Fusion Eng. Des. **74**, 351 (2005).
[11] U. Fantz, P. Franzen, B. Heinemann, and D. Wünderlich, Rev. Sci. Instrum. **85**, 02B305 (2014).
[12] W. Kraus, D. Wünderlich, U. Fantz, B. Heinemann, F. Bonomo, and R. Riedl, Rev. Sci. Instrum. **89**, 052102 (2018).
[13] G. Chitarin, G. Serianni, V. Toigo, M. Bigi, M. Boldrin, S. Dal Bello, L. Grando *et al.,* AIP Conference Proceedings **2052**, 030001 (2018).
[14] M. Boldrin, M. Simon, G. Escudero, G. M. Krohn, H. Decamps, T. Bonicelli, and V. Toigo, Fusion Eng. Des. **146**, 1895 (2019).
[15] V. Toigo, S. Dal Bello, M. Bigi, M. Boldrin, G. Chitarin, L. Grando, A. Luchetta, D. Marcuzzi *et al.,* Nucl. Fusion **59**, 086058 (2019).
[16] R. Hemsworth, H. Decamps, J. Graceffa, B. Schunke, M. Tanaka, M. Dremel, A. Tanga *et al.,* Nucl. Fusion **49**, 045006 (2009).
[17] P. McNeely, H.-D. Falter, U. Fantz, P. Franzen, M. Fröschle, B. Heinemann, W. Kraus, Ch. Martens *et al.,* Rev. Sci. Instrum. **77**, 03A519 (2006).
[18] E. Speth H.D. Falter, P. Franzen, U. Fantz, M. Bandyopadhyay, S. Christ, A. Encheva, M. Fröschle *et al.,* Nucl. Fusion **46**, S220 (2006).
[19] K. Ikeda, K. Tsumori, M. Kisaki, H. Nakano, K. Nagaoka, M. Osakabe, S. Kamio *et al.,* AIP Conference Proceedings **2011**, 060002 (2018).
[20] Y. Takeiri, Y. Oka, M. Osakabe, K. Tsumori, O. Kaneko, T. Takanashi, E. Asano, T. Kawamoto *et al.,* Rev. Sci. Instrum. **68**, 2003 (1997).
[21] H. Hamabe, Y. Takeiri, K. Ikeda, Y. Oka, M. Osakabe, K. Tsumori, E. Asano, T. Kawamoto, *et al.,* Rev. Sci. Instrum. **72**, 3237 (2001).
[22] Y. Takeiri, K. Ikeda, H. Hamabe, M. Osakabe, O. Kaneko, Y. Oka, K. Tsumori, E. Asano, *et al.,* Rev. Sci. Instrum. **73**, 1057 (2002).
[23] K. Tsumori, Y. Takeiri, K. Nagaoka, K. Ikeda, M. Osakabe, Y. Oka, O. Kaneko, M. Shibuya *et al.,* Plasma Sci. and Technol. **8**, 24 (2006).
[24] M. Kisaki, K. Ikeda, M. Osakabe, K. Tsumori, H. Nakano, S. Geng, K. Nagaoka, O. Kaneko, and Y. Takeiri, Rev. Sci. Instrum. **87**, 02B321 (2016).
[25] H. Nakano, K. Tsumori, K. Nagaoka, M. Shibuya, U. Fantz, M. Kisaki, K. Ikeda, M. Osakabe *et al.,* AIP Conference Proceedings **1390**, 359 (2011).
[26] K. Tsumori, H. Nakano, M. Kisaki, K. Ikeda, K. Nagaoka, M. Osakabe, Y. Takeiri, O. Kaneko *et al.,* Rev. Sci. Instrum. **83**, 02B116 (2012).
[27] M. Kisaki, K. Tsumori, S. Geng *et al.,* "Progress of experimental study on negative ion production and extraction", Proceedings of 26th IAEA Fusion Energy Conference, CN234/FIP/1-4, Kyoto, Japan, 17-22 October 2016.
[28] S. Geng, K. Tsumori, H. Nakano, M. Kisaki, Y. Takeiri, M. Osakabe, K. Ikeda, K. Nagaoka *et al.,* Plasma and Fusion Research **10**, 3405016 (2015).
[29] K. Ikeda, H. Nakano, K. Tsumori, M. Kisaki, K. Nagaoka, M. Osakabe, Y. Takeiri, and O Kaneko, New J. Phys. **15**, 103026 (2013).
[30] S. Geng, K. Tsumori, H. Nakano, M. Kisaki, K. Ikeda, M. Osakabe, K. Nagaoka, Y. Takeiri, and M. Shibuya, Fusion Eng. Des. **123**, 481 (2017).
[31] M. Osakabe, Y. Takeiri, K. Tsumori, S. Murakami, O. Kaneko, K. Ikeda, Y. Oka, E. Asano, T. Kawamoto *et al.,* Rev. Sci. Instrum. **72**, 590 (2001).